Research article

A multi-channel *in situ* light scattering instrument utilized for monitoring protein aggregation and liquid dense cluster formation

Sven Falke [a,b,*], Hévila Brognaro [a,c], Arayik Martirosyan [a], Karsten Dierks [d], Christian Betzel [a,b]

[a] University Hamburg, Institute of Biochemistry and Molecular Biology, Laboratory for Structural Biology of Infection and Inflammation, c/o DESY, Build. 22a, Notkestr. 85, 22607, Hamburg, Germany
[b] The Hamburg Center for Ultrafast Imaging, c/o DESY, Luruper Chaussee 149, Hamburg, 22607, Germany
[c] Centre for Free-Electron-Laser Science, c/o DESY, Luruper Chaussee 149, Hamburg, 22607, Germany
[d] Xtal Concepts GmbH, Schnackenburgallee 13, 22525, Hamburg, Germany

ABSTRACT

Liquid-liquid phase separation (LLPS) phenomena have been observed *in vitro* as well as *in vivo* and came in focus of interdisciplinary research activities particularly aiming at understanding the physico-chemical pathways of LLPS and its functionality in recent years. Dynamic light scattering (DLS) has been proven to be a most efficient method to analyze macromolecular clustering in solutions and suspensions with diverse applications in life sciences, material science and biotechnology. For spatially and time-resolved investigations of LLPS, i.e. formation of liquid dense protein clusters (LDCs) and aggregation, a novel eight-channel *in situ* DLS instrument was designed, constructed and applied. The real time formation of LDCs of glucose isomerase (GI) and bovine pancreatic trypsin inhibitor (BPTI) under different physico-chemical conditions was investigated *in situ*. Complex shifts in the particle size distributions indicated growth of LDCs up to the μm size regime. Additionally, near-UV circular dichroism spectroscopy was performed to monitor the folding state of the proteins in the process of LDC formation.

1. Introduction

In recent years liquid dense clusters (LDCs), which are formed by liquid-liquid phase separation (LLPS), gained substantial attention due to their diverse functions in cells [1, 2, 3]. Cellular membrane-less organelles were described as LDCs, which trigger divers processes like stress responses, sorting, transport, storage and activity of macromolecules. LLPS is also linked to the emergence of neurodegenerative diseases, as summarized by Forman-Kay et al. (2018) [4]. Considering that already in the 19th century LLPS was recognized to be a common mechanism in the formation of membrane-less organelles [5] it is remarkable that until now underlying molecular details have only partly been understood. As LDC formation obviously has also a high impact in biochemistry and biotechnology research, a variety of recent experiments has further investigated formation, dynamics, stability and symmetry of LDCs and related assemblies [6, 7, 8] and has also unveiled that various membrane-less organelles are highly dynamic dense liquids formed by a first order phase transition [3, 9]. Furthermore, "super-resolution" fluorescence and electron microscopy as well as X-ray scattering have

identified macromolecule LDC formation in the presence of a variety of polymers and multivalent ions [10, 11, 12, 13]. In this context the flexibility of low-complexity protein domains and RNAs was recognized to promote the formation of LDCs [1, 2]. Analytical techniques, i.e. X-ray tomography and different spectroscopic techniques, have contributed to the identification of individual structural determinants supporting LLPS. Interestingly, structural and dynamic properties of LDCs are also observed in early events of crystal nucleation and proteins inside LDCs undergo density fluctuations based on distinct individual complex formation [14]. Today it is commonly accepted that protein crystallization comprises a two- or multi-step nucleation mechanism, which is harboring an intermediate crowding state of LDCs [12, 15, 16, 17]. For glucose isomerase (D-xylose ketol-isomerase, GI) depletion interactions were induced using different PEGs, which differ in hydrophobicity and molecular weight, as also investigated and reported for other proteins before [18, 19, 20], and intermediate LDCs in the μm size regime were identified prior to local crystal lattice formation inside the clusters [10]. It can be assumed that LDC formation, preceding nucleation, followed by lattice

formation is most common in crystallizations events, even though some exceptions and additions have been reported [21, 22].

Grouazel et al. assessed LLPS of bovine pancreatic trypsin inhibitor (BPTI) at different temperatures using SAXS [23]. Other approaches to investigate the solubility, phase diagram, binodal curve and crystal lattice formation of BPTI include neutron scattering studies [24], X-ray diffraction analysis [25] and fluorescence quenching [26]. The investigations by Veesler et al. and Grouazel et al. also identified and characterized a distinct dependency of pH value and temperature of the protein solution on the clustering and phase transition in much detail [23, 25]. BPTI is of particular medical importance due to its unspecific inhibition of serine proteases. It was utilized for example in cardiac surgery and is capable of reducing blood loss, however unfortunately showed significant negative side effects as well [27, 28]. Interestingly, an uncommon suppression of nucleation in the BPTI dense phase was observed, which was assigned to the high protein concentration, leading to a gel-like state with reduced diffusivity. A strong attractive potential of BPTI decamers formed in solution was indicated in comparison to monomer-monomer interactions at conditions above the temperature boundary curve of LLPS in the phase diagram, as well as a dense phase enriched in decamers [29].

Dynamic light scattering (DLS) is a non-invasive analytical technique that allows determining the size distribution of macromolecules, colloids and other particles based on Brownian motion. It is applicable to different sample environments with comparably low sample consumption. Particle size distributions can be investigated in real-time and optionally in flow mode [30, 31]. The intensity pattern of light scattered by particles in solution is correlated with itself within short time intervals to determine the autocorrelation function (ACF), which allows determining the diffusion constant of the particles via an inverse Laplace transform and allows calculating hydrodynamic radii (R_h) via the Stokes-Einstein equation [32].

Today's most common DLS applications include the characterization of suspensions in life sciences, as well as industrial quality control in material science and biotechnology. One example in structural biology is scoring and optimization of protein solutions prior to crystallization and SAXS experiments [31, 33]. For the experiments described, we designed, constructed and applied a novel and up to now unique *in situ* DLS instrument, which allows simultaneous recording of scattered light in up to eight different positions approx. 280 µm away from each other, covering a distance of 2 mm in total. The distance in between two measurement positions ensures statistical independency of the measurements. The system can be applied to analyze suspensions e.g. along counter-diffusion capillaries, in multi-well plates or in individual droplets. This multi-channel DLS instrument allows highly time efficient data collection and is highly suitable to monitor oligomerization/aggregation processes, particle gradients and inhomogeneities in molecular suspensions, covering a wide regime of particle radii.

For the investigations presented hereafter, the *in situ* DLS instrumentation was calibrated and applied to shed light on LDC formation processes of BPTI and GI. The DLS analyses were complemented by near-UV circular dichroism (CD) spectroscopy to monitor the tertiary structure and in this context the stability of the proteins. The obtained results confirm the feasibility and highlight the potential of *in situ* DLS, particularly of a multi-channel system, to monitor and score protein clustering in combination with CD spectroscopy. Furthermore, distinct preparation and rapid scoring of native LDCs of different protein molecules is considered highly relevant in future imaging approaches in structural biology [34, 35, 36].

2. Material and methods

2.1. Sample preparation

BPTI from bovine lung and *Streptomyces rubiginosus* GI were purchased from Merck (Germany) and Hampton Research (USA),

respectively. The protein purity was verified by SDS-PAGE. For DLS and CD spectroscopy experiments, BPTI dissolved in dH$_2$O (40 mg ml^{-1}; MW: 6.5 kDa; $\varepsilon = 6300$ M^{-1} cm^{-1}) was slowly mixed with 500 mM KSCN (final concentration of 250 mM) in 10 mM sodium acetate pH 4.9 to a final BPTI concentration of 20 mg ml^{-1}. BPTI and KSCN were mixed in a cold bath at the respective temperature. GI (MW: 43 kDa, $\varepsilon = 46.41$ M^{-1} cm^{-1}) was first dialyzed in 10 mM MES pH 6.5 and 500 mM NaCl and mixed at 20 °C with PEG 20′000 to reach a final concentration of 11 % (w/v) for PEG and 10 mg ml^{-1} for GI.

2.2. LDC preparation

Terasaki plates with 72 wells (Thermo Fisher Scientific, USA) were applied to prepare and investigate LDCs. After mixing protein and crowding agent, the plate wells contained 4 µl solution in total, which were covered with a thin layer of Al's oil (Hampton Research, USA) to reduce evaporation. A Leika M 205C stereo microscope (Leica Microsystems, Switzerland) with DIC optics was used to monitor the sample suspensions at low resolution. For rapid protein staining Eosin Scarlet (Jena BioSience GmbH, Germany) was added to LLPS samples.

2.3. DLS

The multichannel DLS instrumentation shown in Figures 1 and 2A-C consists of optical elements defining the light path and scattering geometry around the sample holder as well as a diode laser (Schäfter + Kirchhoff GmbH, Germany) providing 120 mW output power with a wavelength of 660 nm. Furthermore, eight detectors and correlator units are combined in one cabinet together with a CPU for displaying and processing data. Focus optics, objective lens and Faraday isolators are combined to guide the laser light into a single mode fiber cable. A mechanical adjustment mechanism with µm precision allows precise coupling of this laser fiber cable (Schäfter + Kirchhoff GmbH). A collimator of 50 mm focal length, resulting in a minimal beam diameter of 25 µm, was used. The laser light at the fiber output is focused into the sample container mounted onto a black base plate (45 cm × 20 cm). Sample drops were placed inside a glass container and covered with Al's oil. Light scattered by particles in the sample drops is focused onto eight receiver fibers via achromatic lenses. A customized ferrule takes up the eight fibers in a row. With this setup the scattered light emerging from equidistant positions along the laser beam passage through a sample suspension is thus collected by single-mode 4.6 µm core diameter fibers and transmitted to the detector units. An x/y/z-translation step motor control is installed to adjust laser output fiber and receiver optics and to select measurement positions in the sample volume. An additional x/y-translation and rotation hinge allows precise movement of all eight receiver focal points onto the laser beam focal point. Design and construction of all optical elements was performed by XtalConcepts GmbH (Germany). The fiber cables were connected to implemented photomultipliers (Hamamatsu H10682, Japan). The corresponding output signals were transferred to one correlator unit each (XtalConcepts, Germany), which allow processing of decay times from 400 ns up to seconds. The generated data were integrated and processed by customized python-based software for further analysis and display. The ACFs were evaluated using the CONTIN algorithm (Constrained regularization method for inverting data) [32] with no cumulant analysis involved, allowing to directly calculate the diffusion constants and obtain R_h values. If not stated otherwise, experiments were performed at 20 °C.

2.4. CD spectroscopy

The overall tertiary structure conformation and potential structural changes were monitored by following the near-UV CD-spectra of the protein sample solutions applying a Jasco J-815 spectrometer (Jasco, USA) and utilizing a 1 mm quartz cuvette. For each measurement, three spectra with a data point increment of 0.1 nm were averaged. Via a
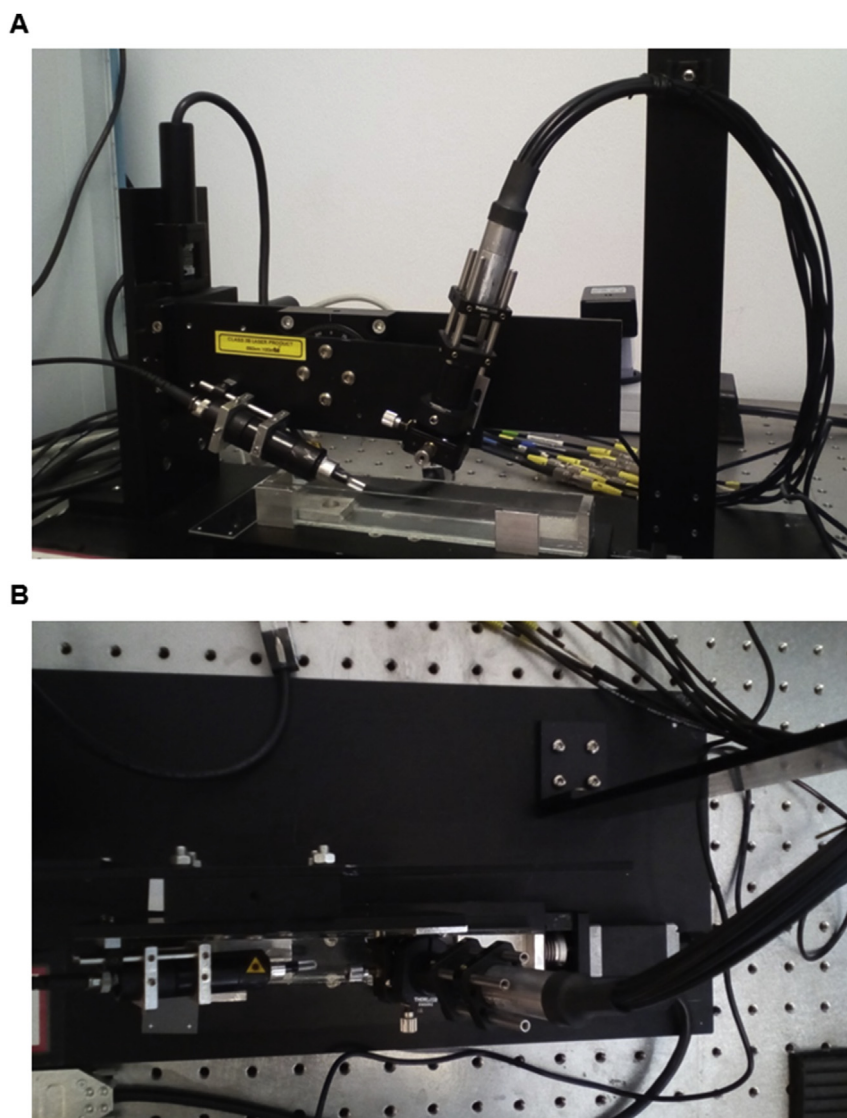
Figure 1. Eight-channel *in situ* DLS setup: Side view (A) and top view (B). Laser and receiver optical elements are shown in a default position adjusted to the sample holder below located on a motorized stage.

Peltier element (Jasco, USA) the temperature was maintained and stabilized at 10 °C to monitor LDC formation of BPTI and at 20 °C to monitor LDC formation of GI. The corresponding solution compositions are specified in section 2.2. In order to investigate the temperature stability of BPTI (40 mg ml^{-1}), the temperature was increased by 1 °C per minute in order to adjust and then stabilize the temperature for the next measurement.

3. Results and discussion

The *in situ* multi-channel DLS system (Figures 1 and 2) described in section 2 was developed and optimized to investigate early stages of macromolecular clustering, biomolecular mass transport phenomena, fibrillation, 2D self-assembly and dis-assembly processes. The instrument is specifically suitable to collect information about size and dynamics of biological assemblies as well as to probe intermolecular interactions in protein clustering processes and early events in crystal nucleation. This DLS system further allows a most time-efficient determination of the diffusion constant by simultaneously collecting scattering signals at up to eight independent neighboring positions in a sample suspension. This DLS device can additionally be applied to identify and monitor local inhomogeneities and local gradients of particle concentrations in a

biomolecular suspension or solution, which cannot be identified by standard single-channel DLS instruments.

Prior to experiments, the sample container, the scattering geometry and optics were aligned and optimized (Figure 2B) and a gold nanoparticle suspension (specified particle radius: 25 nm; Strem chemicals, USA), was used for verification of a reliable particle size determination (Figure 2D/E). The determined diffusion constants were used to calculate R_h. The mean values of R_h determined for the gold nanoparticles by the eight detectors were: 22.4 ± 0.4 nm, 22.2 ± 1.2 nm, 22.9 ± 2.8 nm, 22.4 ± 1.8 nm, 21.9 ± 0.5 nm, 21.9 ± 1.1, 21.9 ± 0.2 nm and 23.1 ± 1.3 nm, showing a deviation of only approx. 5 % from each other.

In preparation for monitoring LDC formation of BPTI (6.5 kDa) by DLS, LLPS was visualized utilizing a stereomicroscope, first applying KSCN to initiate crowding as essentially reported before [29]. The observed BPTI clustering and cluster size distribution depend on the thiocyanate anion and its concentration (Figure 3). Despite the possibility to interact with the protonated amino group of the three lysin side chains of BPTI and its general properties according to the position in the Hofmeister series, SCN$^-$ provides a sufficiently strong "salting out" effect in the aggregation process. Moreover, BPTI LLPS can also be induced by sodium malonate at a temperature higher than the observed critical temperature for LLPS formation when applying KSCN (Figure 3G).
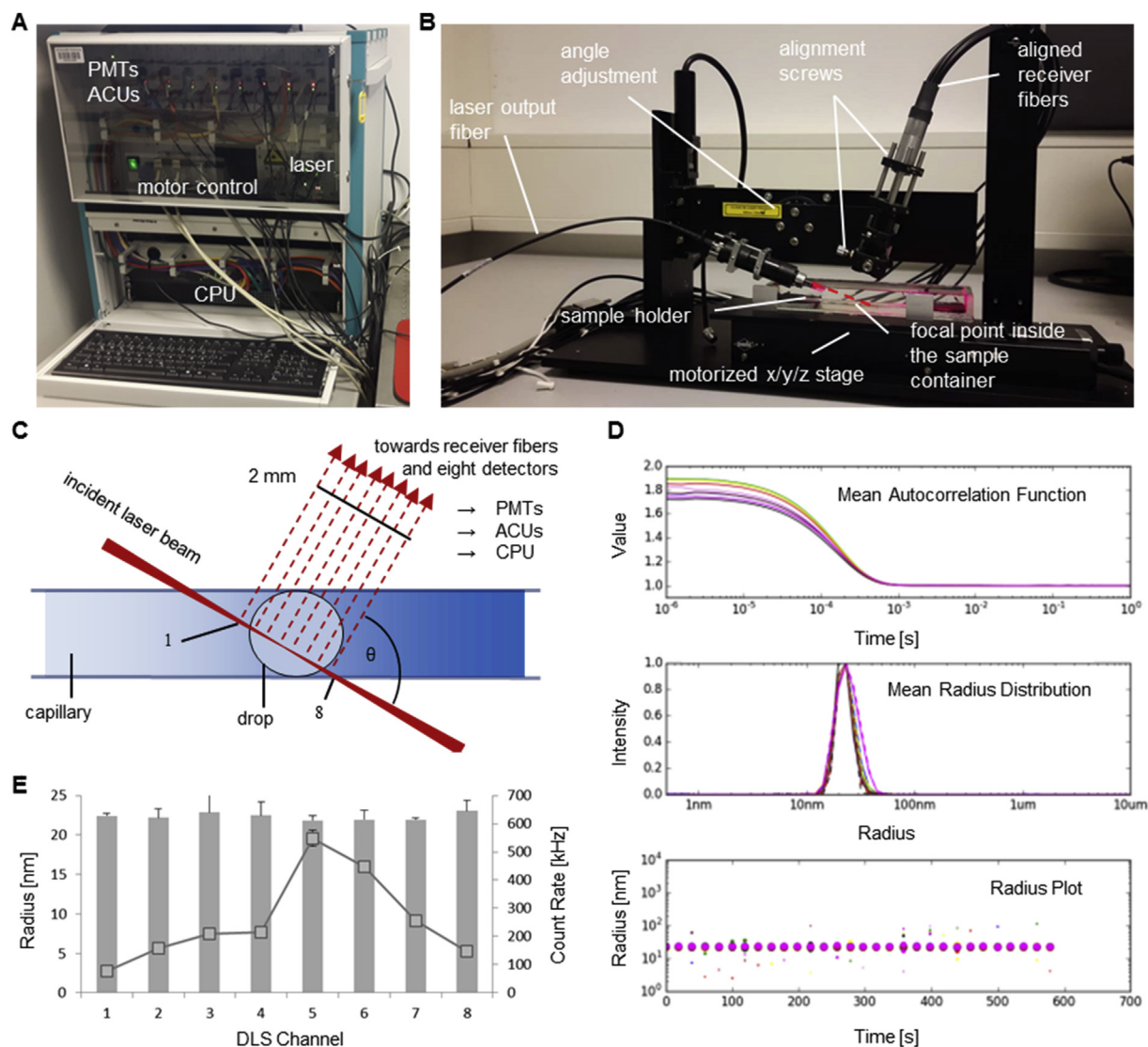
Figure 2. Eight-channel *in situ* DLS setup (A) Portable hardware cabinet, including the diode laser, eight photomultiplier tubes (PMTs) for detection, autocorrelation units (ACUs) and a CPU (B) Setup of laser fiber and receiver optical elements aligned with the sample holder. A thermostat and heating foil below the holder is used for temperature regulation. The laser beam is schematically shown as dashed red line. (Approx. maximum height: 28 cm) (C) Schematic representation of the scattering geometry, measurement positions 1–8 (1 and 8 are labelled) and the eight-channel detection principle (D) Exemplary eight-channel DLS experiment using gold nanoparticles for setup verification. (E) Averaged radii (grey columns) as processed by the individual detectors. The values of the count rates, shown in parallel, approx. fit the expected decrease of scattered light with increasing distance from the focal point of the laser.
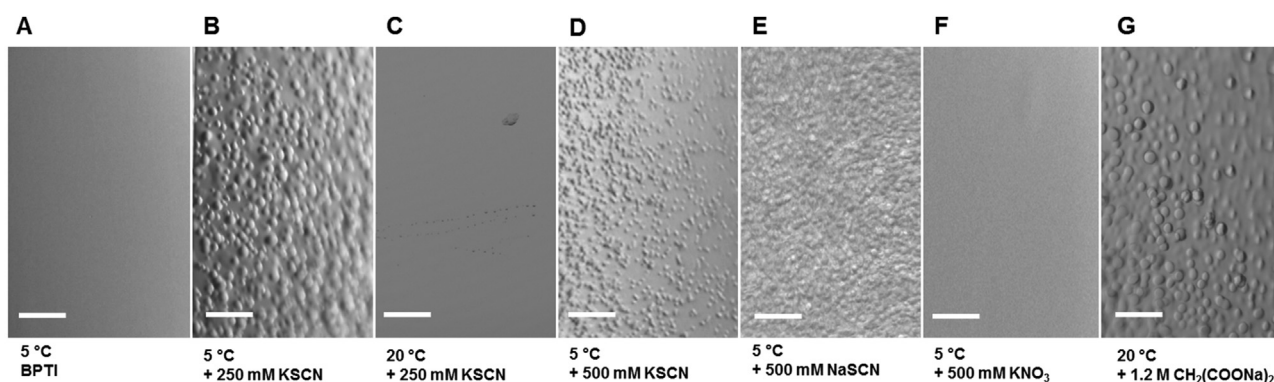

Figure 3. LLPS of BPTI (20 mg ml^{-1}), specifically triggered by SCN$^-$. Variation of the temperature, the SCN$^-$ concentration and the counter ion in individual drops (A–G) allows adjusting the number and size of LDCs in a defined area of the phase diagram. Scale bar: 20 μm.

Malonate ions are known to provide a densely negatively charged environment supporting protein crystallization [37]. According to a

theoretical approach to calculate the effective repulsion energy between protein molecules [38], which is more accurate for small proteins like BPTI, the value of k_BT is varying by several orders of magnitude for BPTI in aqueous solution, depending on the molecule orientation, indicating defined and highly specific oligomerization epitopes, most probably also inside LDCs. A conformational flexibility of BPTI, which also depends on the redox state of the BPTI solution [39], may support the propensity of BPTI to undergo LLPS, which might further be supported by π-π interactions, as suggested for other proteins [40]. Addition of 1 mM DTT to a solution containing 250 mM KSCN prior to mixing with BPTI did however not change the observed LLPS.

To assess LLPS of GI, different molecular weight PEGs ranging from PEG 300 to 20′000 were applied as crowding agents at 20 °C, a temperature at which LDC formation is triggered depending on PEG molecular weight and its concentration. Figure 4 shows GI 20 min after mixing with different PEGs at a final concentration of 11%, including the formation of stable LDCs in the presence of PEG 20′000. Interestingly, high molecular weight PEGs promoted instant LDC formation, while lower molecular weight PEGs forced GI to transit from a clear solution to a crystalline phase without visible intermediate LLPS [41]. This has been investigated recently in detail applying higher concentrations of GI [41]. Data reported shed light on the crystal nucleation pathways of GI in addition to experiments performed by Vivarès et al. [10]. Via cryo-TEM no metastable LDCs as precursor of the crystalline state were observed for different PEGs recently, however, nucleation events were guided by oriented cluster attachments, which are partly crystalline [41].

After calibration, the multi-channel DLS instrumentation was used to comparatively investigate the dynamic processes of LDC formation of both proteins, BPTI and GI, in individual droplets over time (Figure 5). Color-coded radius plots of three data collection channels are shown, which sufficiently cover most of the cross-section of the respective droplet in close proximity to the focal point of the laser and sufficiently characterize the droplets. Figures 5A/D show nearly monodisperse solutions of BPTI ($R_h = 1.8 \pm 0.3$ nm) and tetrameric GI ($R_h = 4.4 \pm 0.3$ nm) respectively. Once the BPTI solution was cooled down to 10 °C and mixed with KSCN solution, initial crowding was detectable after less than 60 s and an additional fraction of particles was observed (approx. 180–230 nm) with slowly further increasing radii up to approx. 350 nm and growing more rapidly after 9 min. However, BPTI monomers and small oligomers were observed to be highly abundant throughout the whole DLS experiment. In contrast to BPTI, GI tetramers were instantaneously crowding, resulting in a predominant fraction of distinct aggregates after PEG 20′000 was added to the droplet. The hydrodynamic radii of aggregates ranged from 30 to 50 nm at this stage. Those particles were slowly doubling their size (16–18 min after mixing) with minor variation comparing different measurement positions, i.e. different detector channels. An additional rapid change in size distribution afterwards indicates further aggregation and formation of highly polydisperse

particles with R_h values of approx. 1 μm or higher. The ratio of particles with an R_h value of approx. 1 μm and particles with $R_h < 100$ μm is slightly different comparing the data of the three channels on display (Figure 5). Comparing the radius plots, only minor differences in local quantity of larger aggregates and minor delays of the clustering process are indicated for different neighboring measurement positions in the droplet for both proteins respectively.

For BPTI, monomeric protein and small oligomers were still highly abundant and coexist after much larger clusters have formed towards the end of the LLPS process. In protein crystallization, initial formation of a few multimeric clusters with critical size, which are coalescing and further growing in size, presents an early stage of nucleation [12, 42]. This process was followed by sedimentation of larger particles and initial gain of order. The observed size distribution pattern of 2–3 distinct particle species during the early events of nucleation appears to be a highly individual feature based on intermolecular interactions during LLPS. Furthermore, for analyzing clusters larger than approx. 1–2 μm and analyzing almost intransparent suspensions, the application of diffusing-wave spectroscopy or cross-correlation light scattering was recommended for a most reliable size determination [43, 44].

Complementing multi-channel DLS experiments the structural integrity of BPTI and GI was investigated applying near-UV CD spectroscopy (Figure 6). Previously, a change of the α-helical structure content of prion protein during hydrogel formation was reported [45] and for BSA a specific change of its secondary structure and folding stability was reported upon addition of PEG [46]. Near-UV CD spectroscopy generally provides a distinct tertiary structure "fingerprint", which is specifically sensitive to aromatic amino acids and disulfide bonds [47]. BPTI consists of 58 amino acids, containing four tyrosine residues in total, three of them are part of two neighboring β-sheet regions supporting intermolecular interactions [48]. CD spectroscopy data collected in the tyrosine-sensitive region of the spectrum do not indicate any rearrangements of their position along the process of LDC formation at 10 °C (Figure 6A) confirming a stable tertiary structure fold throughout the experiment. Data collected for GI before and after inducing LDC formation by PEG 20′000 as crowding agent also showed no significant change in overall protein conformation during LDC formation (Figure 6C). GI consists of 388 amino acids including six tryptophan residues, nine tyrosine residues and 23 phenylalanine residues distributed throughout the sequence, which predominantly determined the ellipticity that was recorded. For BPTI the temperature induced denaturation process with the highest loss of ellipticity (dθ/dT) in the near-UV regime (around 275 nm) at approx. 80 °C is shown for comparison (Figure 6B) and results in amorphous precipitation of BPTI. The minor differences observed in the spectra recorded at 5° and 25°C (Figure 6B) are not supposed to significantly influence the observed temperature specificity of BPTI to undergo LLPS upon mixing with KSCN only at temperatures ≤15 °C.
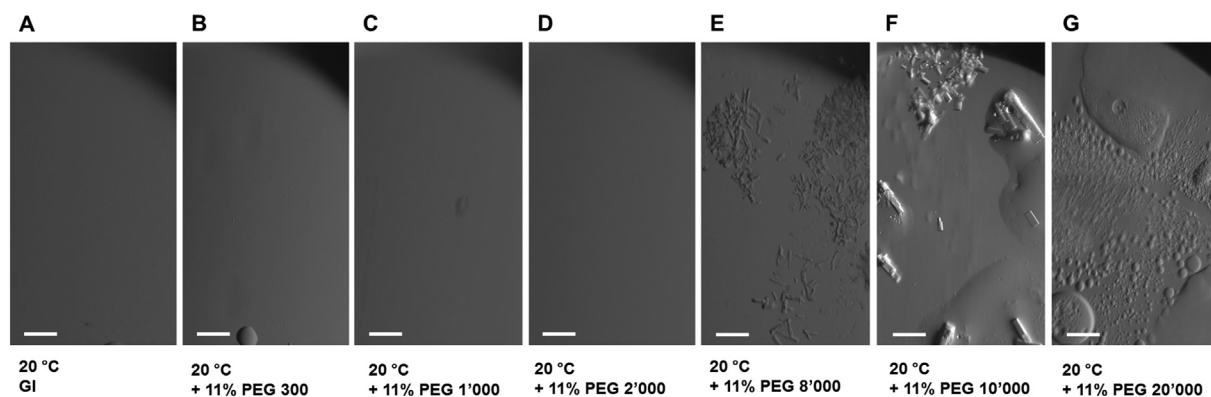

Figure 4. Phase states and LLPS of GI (10 mg ml^{-1}) in the presence of 11% (w/v) PEG of different molecular weights (A–G). Images were recorded 20 min after mixing. Crystals formed in the presence of PEG 8′000 and PEG 10′000 (E–F). Scale bar: 40 μm.
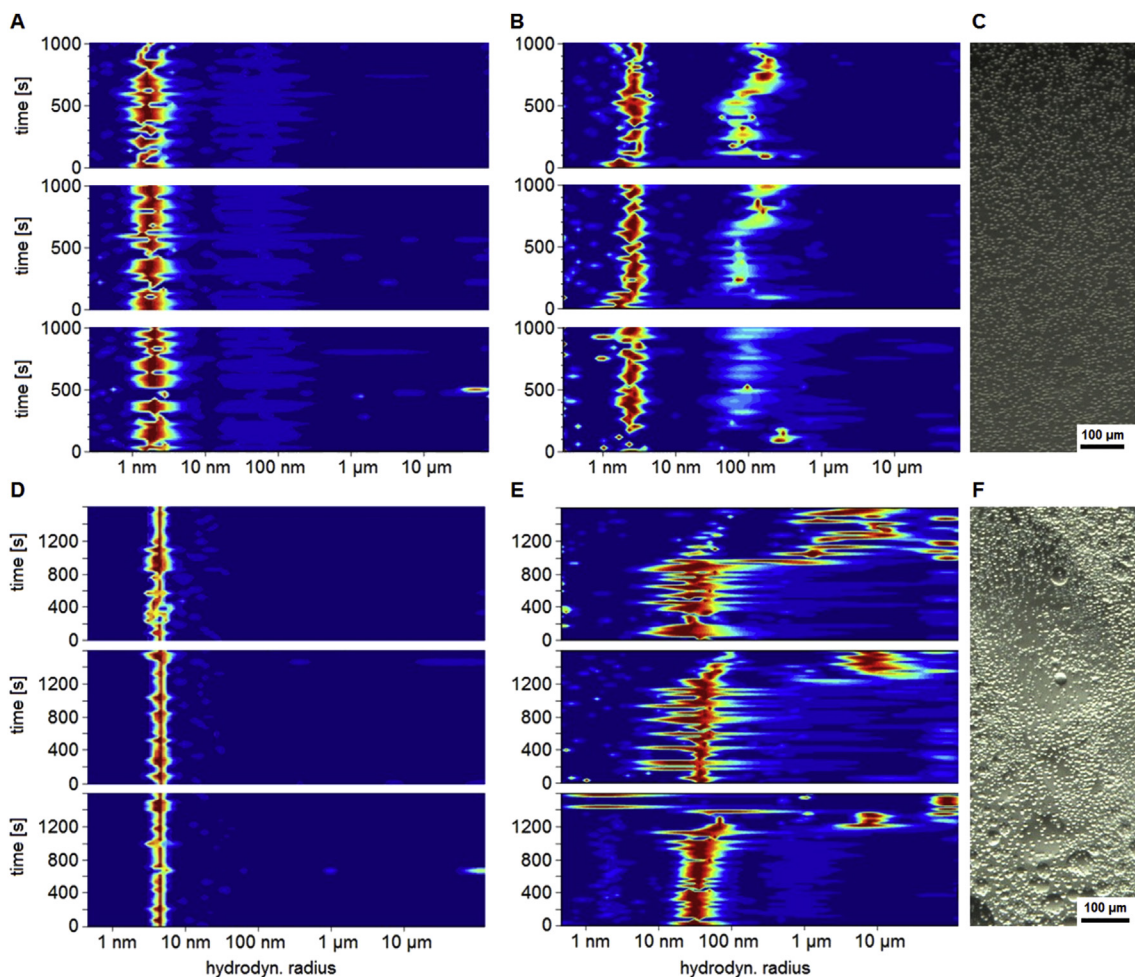
Figure 5. Real-time monitoring of LDC formation applying multi-channel DLS: BPTI (A–B) and GI (D–E): Radius distribution plot of BPTI (A), comparing exemplary three data collection channels and GI (D), with protein only at 20 °C as well as after mixing BPTI with KSCN at 10 °C (B) and mixing GI with PEG 20'000 (E) respectively. The individual radius plots are indicating differences in abundancy of particle species depending on the position of the measurement at different time points of cluster formation (B/E). Micrographs showing LDCs of BPTI at 10 °C (C) and GI at 20 °C, 20 min after mixing (F).

In summary, the application examples presented demonstrate the potential of a newly designed *in situ* DLS system, allowing monitoring the formation of LDCs, as well as any other macromolecular oligomerization/aggregation with improved spatial and temporal resolution in a range of different sample containers. This hardware will allow experimentally analyzing molecular mass transport and specific growth of molecular

assembles *in vitro* in more detail. Particular sample containers, like microfluidic mixing chips as used in serial X-ray crystallography data collection [49] can be combined with the current multichannel DLS setup to monitor oligomerization prior to diffraction data collection. As demonstrated, multi-channel DLS and CD spectroscopy can be combined to obtain complementary information about macromolecular clustering
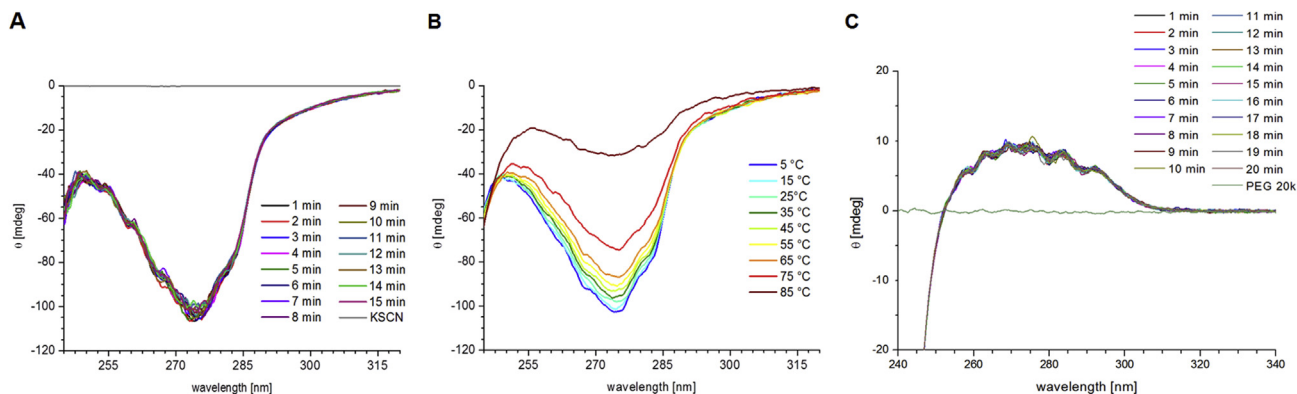

Figure 6. Monitoring of the tertiary structure integrity during the clustering process using near-UV CD spectroscopy. The LLPS process of BPTI at 10 °C (A) and GI at 20 °C (C) is continuously monitored. Thermal denaturing of BPTI is shown for comparison (B). The tertiary structure of BPTI is changing upon a temperature decrease from 25 °C down to 5 °C, indicated by a slight ellipticity change in the tyrosine-sensitive region of the spectrum.

and potential structural changes of the respective proteins. The adherence of the tertiary structure during protein LDC formation is underlining the potential of LDCs to be applied in upcoming innovative hybrid methods for high resolution and time-resolved structural investigations.

Declarations

Author contribution statement

Sven Falke: Conceived and designed the experiments; Performed the experiments; Analyzed and interpreted the data; Wrote the paper.

Christian Betzel: Conceived and designed the experiments; Wrote the paper.

Karsten Dierks: Conceived and designed the experiments; Contributed reagents, materials, analysis tools or data.

Hévila Brognaro: Performed the experiments.

Arayik Martirosyan: Performed the experiments; Analyzed and interpreted the data.

Competing interest statement

The authors declare no conflict of interest.

Additional information

No additional information is available for this paper.

References

[1] A.A. Hyman, C.A. Weber, F. Jülicher, Liquid-liquid phase separation in biology, Annu. Rev. Cell Dev. Biol. 30 (2014) 39–58.

[2] R.J. Wheeler, A.A. Hyman, Controlling compartmentalization by non-membrane-bound organelles, Philos. Trans. R. Soc. Biol. Sci. 373 (2018), 20170193.

[3] S. Alberti, A. Gladfelter, T. Mittag, Considerations and challenges in studying liquid-liquid phase separation and biomolecular condensates, Cell 176 (2019) 419–434.

[4] J.D. Forman-Kay, R.W. Kriwacki, G. Seydoux, Phase separation in biology and disease, J. Mol. Biol. 430 (2018) 4603–4606.

[5] A. Dröscher, B. Edmund, Wilson's the cell and cell theory between 1896 and 1925, Hist, Philos. Life Sci. 24 (2002) 357–389.

[6] D.G. Greene, S. Modla, N.J. Wagner, S.I. Sandler, A.M. Lenhoff, Local crystalline structure in an amorphous protein dense phase, Biophys. J. 109 (2015) 1716–1723.

[7] R.M.L. Queiroz, T. Smith, E. Villanueva, M. Marti-Solano, M. Monti, M. Pizzinga, D.-M. Mirea, M. Ramakrishna, R.F. Harvey, V. Dezi, G.H. Thomas, A.E. Willis, K.S. Lilley, Comprehensive identification of RNA–protein interactions in any organism using orthogonal organic phase separation (OOPS), Nat. Biotechnol. 37 (2019) 169–178.

[8] T.M. Franzmann, S. Alberti, Prion-like low-complexity sequences: key regulators of protein solubility and phase behavior, J. Biol. Chem. 294 (2019) 7128–7136.

[9] A. Narayanan, A.B. Meriin, M.Y. Sherman, I.I. Cisse, A first order phase transition underlies the formation of sub-diffractive protein aggregates in mammalian cells, BioRxiv (2017).

[10] D. Vivarès, E.W. Kaler, A.M. Lenhoff, Quantitative imaging by confocal scanning fluorescence microscopy of protein crystallization via liquid-liquid phase separation, Acta Crystallogr. D Biol. Crystallogr. 61 (2005) 819–825.

[11] S. Da Vela, M.K. Braun, A. Dörr, A. Greco, J. Möller, Z. Fu, F. Zhang, F. Schreiber, Kinetics of liquid-liquid phase separation in protein solutions exhibiting LCST phase behavior studied by time-resolved USAXS and VSANS, Soft Matter 12 (2016) 9334–9341.

[12] R. Schubert, A. Meyer, D. Baitan, K. Dierks, M. Perbandt, C. Betzel, Real-time observation of protein dense liquid cluster evolution during nucleation in protein crystallization, Cryst. Growth Des. 17 (2017) 954–958.

[13] O. Matsarskaia, F. Roosen-Runge, G. Lotze, J. Möller, A. Mariani, F. Zhang, F. Schreiber, Tuning phase transitions of aqueous protein solutions by multivalent cations, Phys. Chem. Chem. Phys. 20 (2018) 27214–27225.

[14] W. Pan, P.G. Vekilov, V. Lubchenko, Origin of anomalous mesoscopic phases in protein solutions, J. Phys. Chem. B 114 (2010) 7620–7630.

[15] M.A. Vorontsova, D. Maes, P.G. Vekilov, Recent advances in the understanding of two-step nucleation of protein crystals, Faraday Discuss 179 (2015) 27–40.

[16] F. Zhang, Nonclassical nucleation pathways in protein crystallization, J. Phys. Condens. Matter 29 (2017) 443002.

[17] P.G. Vekilov, The two-step mechanism of nucleation of crystals in solution, Nanoscale 2 (2010) 2346–2357.

[18] M. Budayova, F. Bonneté, A. Tardieu, P. Vachette, Interactions in solution of a large oligomeric protein, J. Cryst. Growth 196 (1999) 210–219.

[19] D. Vivarès, F. Bonneté, Liquid−Liquid phase separations in urate oxidase/PEG mixtures: characterization and implications for protein crystallization, J. Phys. Chem. B 108 (2004) 6498–6507.

[20] J. Wu, C. Zhao, W. Lin, R. Hu, Q. Wang, H. Chen, L. Li, S. Chen, J. Zheng, Binding characteristics between polyethylene glycol (PEG) and proteins in aqueous solution, J. Mater. Chem. B. 2 (2014) 2983.

[21] K.Wm. Hall, S. Carpendale, P.G. Kusalik, Evidence from mixed hydrate nucleation for a funnel model of crystallization, Proc. Natl. Acad. Sci. U. S. A 113 (2016) 12041–12046.

[22] T. Yamazaki, Y. Kimura, P.G. Vekilov, E. Furukawa, M. Shirai, H. Matsumoto, A.E.S. Van Driessche, K. Tsukamoto, Two types of amorphous protein particles facilitate crystal nucleation, Proc. Natl. Acad. Sci. U. S. A 114 (2017) 2154–2159.

[23] S. Grouazel, F. Bonneté, J.-P. Astier, N. Ferté, J. Perez, S. Veesler, Exploring bovine pancreatic trypsin inhibitor phase transitions, J. Phys. Chem. B 110 (2006) 19664.

[24] M. Budayova-Spano, S. Lafont, J.-P. Astier, C. Ebel, S. Veesler, Comparison of solubility and interactions of aprotinin (BPTI) solutions in H2O and D2O, J. Cryst. Growth 217 (2000) 311–319.

[25] S. Veesler, N. Fertè, M.-S. Costes, M. Czjzek, J.-P. Astier, Temperature and pH effect on the polymorphism of aprotinin (BPTI) in sodium bromide solutions, Cryst. Growth Des. 4 (2004) 1137–1141.

[26] H. Jozawa, Md.G. Kabir, T. Zako, M. Maeda, K. Chiba, Y. Kuroda, Amorphous protein aggregation monitored using fluorescence self-quenching, FEBS Lett. 590 (2016) 3501–3509.

[27] N. Okur, D. Özdemir, Ş. Kahyaoğlu, Z. Şenyiğit, M. Aşıkoğlu, L. Genç, H. Karasulu, Assessment of aprotinin loaded microemulsion formulations for parenteral drug delivery: preparation, characterization, in vitro release and cytotoxicity studies, Curr. Drug Deliv. 12 (2015) 668–679.

[28] J.L. Kristeller, B.P. Roslund, R.F. Stahl, Benefits and risks of aprotinin use during cardiac surgery, Pharmacotherapy 28 (2008) 112–124.

[29] S. Grouazel, J. Perez, J.P. Astier, F. Bonneté, S. Veesler, BPTI liquid-liquid phase separation monitored by light and small angle X-ray scattering, Acta Crystallogr. D Biol. Crystallogr. 58 (2002) 1560–1563.

[30] T.W. Taylor, C.M. Sorensen, Gaussian beam effects on the photon correlation spectrum from a flowing Brownian motion system, Appl. Opt. 25 (1986) 2421–2426.

[31] S. Falke, K. Dierks, C. Blanchet, M. Graewert, F. Cipriani, R. Meijers, D. Svergun, C. Betzel, Multi-channel in situ dynamic light scattering instrumentation enhancing biological small-angle X-ray scattering experiments at the PETRA III beamline P12, J. Synchrotron Radiat. 25 (2018) 361–372.

[32] S.W. Provencher, CONTIN: a general purpose constrained regularization program for inverting noisy linear algebraic and integral equations, Comput. Phys. Commun. 27 (1982) 229–242.

[33] K. Dierks, A. Meyer, H. Einspahr, C. Betzel, Dynamic light scattering in protein crystallization droplets: adaptations for analysis and optimization of crystallization processes, Cryst. Growth Des. 8 (2008) 1628–1634.

[34] M.F. Hantke, D. Hasse, F.R.N.C. Maia, T. Ekeberg, K. John, M. Svenda, N.D. Loh, A.V. Martin, N. Timneanu, D.S.D. Larsson, G. van der Schot, G.H. Carlsson, M. Ingelman, J. Andreasson, D. Westphal, M. Liang, F. Stellato, D.P. DePonte, R. Hartmann, N. Kimmel, R.A. Kirian, M.M. Seibert, K. Mühlig, S. Schorb, K. Ferguson, C. Bostedt, S. Carron, J.D. Bozek, D. Rolles, A. Rudenko, S. Epp, H.N. Chapman, A. Barty, J. Hajdu, I. Andersson, High-throughput imaging of heterogeneous cell organelles with an X-ray laser, Nat. Photonics 8 (2014) 943–949.

[35] M. Rose, S. Bobkov, K. Ayyer, R.P. Kurta, D. Dzhigaev, Y.Y. Kim, A.J. Morgan, C.H. Yoon, D. Westphal, J. Bielecki, J.A. Sellberg, G. Williams, F.R.N.C. Maia, O.M. Yefanov, V. Ilyin, A.P. Mancuso, H.N. Chapman, B.G. Hogue, A. Aquila, A. Barty, I.A. Vartanyants, Single-particle imaging without symmetry constraints at an X-ray free-electron laser, IUCrJ 5 (2018) 727–736.

[36] H. Wang, X. Yan, H. Aigner, A. Bracher, N.D. Nguyen, W.Y. Hee, B.M. Long, G.D. Price, F.U. Hartl, M. Hayer-Hartl, Rubisco condensate formation by CcmM in β-carboxysome biogenesis, Nature 566 (2019) 131–135.

[37] A. Mcpherson, A comparison of salts for the crystallization of macromolecules, Protein Sci. 10 (2001) 418–422.

[38] X. Song, X. Zhao, The van der Waals interaction between protein molecules in an electrolyte solution, J. Chem. Phys. 120 (2004) 2005–2009.

[39] D. Amir, E. Haas, Reduced bovine pancreatic trypsin inhibitor has a compact structure, Biochemistry 27 (1988) 8889–8893.

[40] R.M. Vernon, P.A. Chong, B. Tsang, T.H. Kim, A. Bah, P. Farber, H. Lin, J.D. Forman-Kay, Pi-Pi contacts are an overlooked protein feature relevant to phase separation, ELife 7 (2018).

[41] A.E.S. Van Driessche, N. Van Gerven, P.H.H. Bomans, R.R.M. Joosten, H. Friedrich, D. Gil-Carton, N.A.J.M. Sommerdijk, M. Sleutel, Molecular nucleation mechanisms and control strategies for crystal polymorph selection, Nature 556 (2018) 89–94.

[42] H. Brognaro, S. Falke, C. Nzanzu Mudogo, C. Betzel, Multi-step concanavalin A phase separation and early-stage nucleation monitored via dynamic and depolarized light scattering, Crystals 9 (2019) 620.

[43] P. Zakharov, F. Cardinaux, F. Scheffold, Multispeckle diffusing-wave spectroscopy with a single-mode detection scheme, Phys. Rev. E. 73 (2006).

[44] M. Medebach, C. Moitzi, N. Freiberger, O. Glatter, Dynamic light scattering in turbid colloidal dispersions: a comparison between the modified flat-cell light-scattering instrument and 3D dynamic light-scattering instrument, J. Colloid Interface Sci. 305 (2007) 88–93.

[45] M.A. Kostylev, M.D. Tuttle, S. Lee, L.E. Klein, H. Takahashi, T.O. Cox, E.C. Gunther, K.W. Zilm, S.M. Strittmatter, Liquid and hydrogel phases of PrPC linked to conformation shifts and triggered by alzheimer's amyloid-β oligomers, Mol. Cell 72 (2018) 426–443, e12.

[46] S. Rawat, C. Raman Suri, D.K. Sahoo, Molecular mechanism of polyethylene glycol mediated stabilization of protein, Biochem. Biophys. Res. Commun. 392 (2010) 561–566.

[47] S.B. Jasim, Z. Li, E.E. Guest, J.D. Hirst, DichroCalc: improvements in computing protein circular dichroism spectroscopy in the near-ultraviolet, J. Mol. Biol. 430 (2018) 2196–2202.

[48] A. Wlodawer, J. Nachman, G.L. Gilliland, W. Gallagher, C. Woodward, Structure of form III crystals of bovine pancreatic trypsin inhibitor, J. Mol. Biol. 198 (1987) 469–480.

[49] Y. Gicquel, R. Schubert, S. Kapis, G. Bourenkov, T. Schneider, M. Perbandt, C. Betzel, H.N. Chapman, M. Heymann, Microfluidic chips for in situ crystal X-ray diffraction and in situ dynamic light scattering for serial crystallography, J. Vis. Exp. (2018) 57133.